JGR Space Physics

RESEARCH ARTICLE
10.1029/2021JA029308

Key Points:

- Near-relativistic electron fluxes associated with storms are highly correlated ($r^2 > 0.8$) cross-L^* outside the minimum plasmapause location
- Electron fluxes inside the minimum location of the plasmapause are also well correlated but show little correlation with fluxes outside
- During storm main and recovery phases, the electron fluxes are well correlated across all L^* irrespective of the plasmapause location

Correspondence to:

S. D. Walton,
samuel.walton.18@ucl.ac.uk

Citation:

Walton, S. D., Forsyth, C., Rae, I. J., Watt, C. E. J., Thompson, R. L., Horne, R. B., et al. (2021). Cross-L^* coherence of the outer radiation belt during storms and the role of the plasmapause. *Journal of Geophysical Research: Space Physics*, *126*, e2021JA029308. https://doi.org/10.1029/2021JA029308

Received 2 MAR 2021
Accepted 9 SEP 2021

Cross-L^* Coherence of the Outer Radiation Belt During Storms and the Role of the Plasmapause

S. D. Walton[1], C. Forsyth[1], I. J. Rae[2], C. E. J. Watt[2], R. L. Thompson[3], R. B. Horne[4], N. P. Meredith[4], C. J. Rodger[5], M.-T. Walach[6], M. A. Clilverd[4], and S. A. Glauert[4]

[1]Mullard Space Science Laboratory, University College London, Dorking, UK, [2]Department of Maths, Physics and Electrical Engineering, Northumbria University, Newcastle upon Tyne, UK, [3]Department of Mathematics, University of Reading, Reading, UK, [4]British Antarctic Survey, Cambridge, UK, [5]Department of Physics, University of Otago, Dunedin, New Zealand, [6]Physics Department, Lancaster University, Lancaster, UK

Abstract The high energy electron population in Earth's outer radiation belt is extremely variable, changing by multiple orders of magnitude on timescales that vary from under an hour to several weeks. These changes are typically linked to geomagnetic activity such as storms and substorms. In this study, we seek to understand how coherent changes in the radiation belt are across all radial distances, in order to provide a spatial insight into apparent global variations. We do this by calculating the correlation between fluxes on different L^* measured by the PET instrument aboard the SAMPEX spacecraft for times associated with 15 large storms. Our results show that during these times, variations in the >0.63 MeV electron flux are coherent outside the minimum plasmapause location and also coherent inside the minimum plasmapause location, when flux is present. However, variations in the electron fluxes inside the plasmapause show little correlation with those outside the plasmapause. During storm recovery and possibly main phases, flux variations are coherent across all L^* regardless of plasmapause location, due to a rapid decrease, followed by an increase in radiation belt fluxes across all L^*.

1. Introduction

The outer Van Allen radiation belt is a toroidal region of highly energetic electrons residing in the Earth's inner magnetosphere. It extends from ≈2.5 to 8.0 Earth Radii (R_E) (Van Allen, 1958, 1959), and highly spatially and temporarily variable due to constant competition between enhancement and loss processes (e.g., Friedel et al., 2002). Enhancement occurs as a result of the injection of particles from the outer magnetosphere which become unstable due to electromagnetic wave growth and by resultant wave-particle interactions (Thorne, 2010). The subsequent waves energize the local particle population up to many MeV energies (e.g., Horne & Thorne, 1998; Horne, Thorne, Glauert, et al., 2005; Shprits et al., 2013; Thorne, 2010). Particles can also become energized as a result of inward radial diffusion of hot plasma populations (e.g., Lejosne & Kollmann, 2020; Mann et al., 2016). Particle interactions with waves can also result in the scattering of particles into the local bounce loss cone (the loss cone defined by the magnetic field strength at the base of the field line) or the drift loss cone (the largest bounce loss cone on a given drift path). Drifting particles can also be lost due to a compressed magnetopause intersecting their drift paths (magnetopause shadowing), or drifting around to open field lines on the nightside (losses extensively reviewed in Friedel et al., 2002; Millan & Thorne, 2007). Studies (e.g., Brito et al., 2015; Rae et al., 2018) have also shown that ULF wave modulation of the loss cone can drive enhanced precipitation of radiation belt electrons without any additional requirement for gyro-resonant wave-particle interaction. Fermi acceleration (Fermi, 1949) has also been associated with electron precipitation (Brito et al., 2015).

A globally coherent outer radiation belt is a strong indicator of the nature and extent of various processes acting upon them. When examining the spatial variation of high-energy particles in a planetary environment, it is useful to do so in a magnetic field-based coordinate system such as the L-shell parameter, which is the equatorial distance in R_E to a given dipole-approximated field line. This can also be calculated in a distorted dipole using the International Geomagnetic Reference Field (IGRF). Roederer (1967) describes a similar, though much more complex coordinate system utilizing more realistic magnetic field models to numerically calculate particle drift shells, conserving the third adiabatic invariant. The coordinate L^*

("L-star") is favored further out in the magnetosphere and during periods of heightened activity where the field is more distorted from the dipole approximation, however L^* values at a given location can be vary depending on the particular field model used (Albert et al., 2018; Thompson et al., 2020). Typically, dipole L-shells and L^*-shells deviate more at greater distances from the Earth. Coordinate systems are reviewed in Roederer and Lejosne (2018).

Baker et al. (2001) investigated the electron flux for the entire ($2.5 \leq L \leq 6.5$) outer belt, comparing measurements from the Solar Anomalous Magnetospheric Particle Explorer (SAMPEX) spacecraft (low-Earth orbit [LEO]) to Polar (high-altitude, elliptical orbit). In a 1-year interval, virtually all features were seen by both spacecraft, demonstrating cross-altitude coherence. Results from Kanekal et al. (2001) compared and cross-correlated 2-year of multi-satellite data at a range of altitudes and across a range of L-shells (assumed to be calculated using the IGRF model), finding similar behavior at all locations and further evidence of the coherent nature of the outer belt. Chen et al. (2016) explored this further, to find significant cross-energy (MeV vs. 100s keV), cross-pitch angle (trapped vs. precipitating) coherence in outer belt electrons. This may be a natural consequence of the dominance of wave-particle interactions in the region. Confidence that there is an intrinsic relationship between electrons observed at LEO and those at other altitudes, energies and pitch angles allows its use in nowcasting and forecasting of global radiation belt behavior (Chen et al., 2016). Artificial neural networks (Claudepierre & O'Brien, 2020) and predictive models (Chen et al., 2019) further take advantage of global coherence, using the POES spacecraft to provide inputs, assessed by the Van Allen Probes and measurements made at geosynchronous orbit altitudes.

Early studies of radiation belt coherence (Baker et al., 2001; Kanekal et al., 2001) formed the basis of the Radiation Belt Content (RBC) index (Baker, Kanekal, & Blake, 2004) which integrated the apparent 1.5–6.0 MeV flux across $L = 2.5$–6.5. Correlation of RBC with SAMPEX, Polar, GOES, and HEO spacecraft flux measurements further shows a coherent outer radiation belt. More recently, the Total Radiation Belt Electron Content (TRBEC) index (detailed in Boyd, 2016) has been developed using phase space density data from the Van Allen Probes in the L^*, K, μ adiabatic invariant coordinate system. Using data in this way removes the adiabatic variations that result from examining particles within a set energy range but traversing a region with varying magnetic field strengths. These are useful indices for analyzing the net global change of the outer belt. Murphy et al. (2018) produced a superposed epoch analysis of 73 geomagnetic storms, using TRBEC categorized by several fixed μ. This showed a coherent net decrease, then increase in electron content across μ. Murphy et al. (2020) used the RBC index to examine net changes in electron content over a longer period of time, arguing that the reduced dimensionality is ideal for statistical studies. Global content indices do however, hide the details of spatial variations across L or L^* in the changes of the belts and thus, local physical mechanisms for this variation. It is therefore important to understand when and where the variations in the radiation belt at different L^* are largely coherent or incoherent. In a coherent radiation belt, global content indices would be reflective of enhancement and/or loss processes but in an incoherent belt, interpretation would be more difficult. Due to the short (≈10 min) drifts of near-relativistic outer radiation belt electrons, we assume MLT-dependent variations.

Often overlapping with the outer radiation belt is the cold (1 eV) and more dense (100–10,000 cm^{-3}) plasmasphere. The plasmasphere is essentially an extension of the ionosphere that becomes trapped on magnetic field lines and corotates (Lemaire et al., 1998). The outer boundary of the plasmasphere is known as the plasmapause and while generally not always well defined, can often be characterized by a steep plasma density gradient of at least half an order of magnitude in less than 1 R_E (Carpenter, 1963, 1966; Gringauz, 1963). Typically, the plasmapause is located between 3.0 and 6.0 R_E, although this location varies with geomagnetic activity and local time (Carpenter, 1963, 1966). During periods of high geomagnetic activity, the plasmapause location can come within 1 R_E of the surface of the Earth (e.g., Baker, Kanekal, Li, et al., 2004). The super-position of corotation and convection electric field results in significant local time asymmetry and contribute to the formation of plasmaspheric drainage plumes during many storms, extending from the main body of the plasmapause to the outer magnetosphere (e.g., Goldstein et al., 2004).

Inside the plasmasphere, whistler-mode hiss waves are a prominent and very effective loss mechanism (Abel & Thorne, 1998a, 1998b; Meredith et al., 2007), primarily responsible for the formation of the slot region between the inner and outer radiation belt (Lyons & Thorne, 1973; Lyons et al., 1972). Plasmaspheric hiss is enhanced during geomagnetically active times (Meredith et al., 2004; Smith et al., 1974; Thorne et al., 1973;

Tsurutani et al., 1975), but persists during quiet times (Carpenter, 1978; Thorne et al., 1977). Outside the plasmapause, a strong source of both enhancements and losses are very low frequency (VLF, 100 Hz–10s kHz) whistler-mode chorus waves (Meredith et al., 2020). They originate during cyclotron resonant interactions with plasma sheet electrons that are injected into the inner magnetosphere during enhanced convection (Hwang et al., 2007; Lyons et al., 2005). Multiple studies (e.g., Ozeke et al., 2018, 2019, 2020) also demonstrate the role of Ultra-Low Frequency (ULF) in both fast acceleration and loss of relativistic electrons as low as the inner extent of the outer radiation belt (L≈2.5). Relative contribution of the various processes is currently an active area of discussion (Mann et al., 2016, 2018; Shprits et al., 2013, 2018). Multiple studies (Darrouzet et al., 2013; Hardman et al., 2015; Li et al., 2006; Lichtenberger et al., 2013; Whittaker et al., 2014) suggest that the plasmapause boundary can be seen in the time varying trapped electron fluxes due to the disparity in processes inside and outside.

The L-dependence of electron dynamics in the outer radiation belt, due to many influences including that of the plasmasphere, means that some of the global indices described above may not be entirely representative during periods of high geomagnetic activity. Vassiliadis et al. (2002, 2003) used a two-point correlation function (correlation matrix) to analyze spatial coherence between $L = 1$–10 over 8 years. These studies reveal structured coherent regions in flux variations are categorized into the slot ("S") region between $L = 2$–3, P_0, P_1 regions between $L = 3$–4 and 4–8 respectively, containing the majority of outer belt electrons, and P_2 region between $L = 8$–10, suggesting consistent differences in these regions to each other over the 8 years. This and further work (Vassiliadis, 2008; Vassiliadis et al., 2004, 2005) has associated the different regions with varying response to solar wind speed.

Here, we use a similar method to that in Vassiliadis et al. (2003) (also used in Cosgrove & Sanchez, 2012) to evaluate how well variations in outer radiation belt flux are correlated (and therefore coherent) across L^* during much shorter periods associated with geomagnetic storms. Data from the Proton/Electron Telescope (PET) instrument aboard the SAMPEX spacecraft are used, measuring >0.63 MeV electron flux (energy range discussed below). Given that L^* varies with pitch angle, as well as considering the large angular acceptance of PET, we examine how L^* varies across the PET field of view. In Sections 2.4 and 2.5, we present case studies of two geomagnetic storms (May 1998 and November 2003), analyzing the changing coherence of flux variations throughout the days preceding and following minimum Sym-H. We find that the correlation of the electron flux at different L^* is dependent on the location of the minimum extent of the plasmapause. In Section 2.6 we provide a more statistical approach by averaging the analysis over 15 large storms, which reinforces the key findings from the case studies.

2. Instrumentation and Data Analysis

In this study, we use data from the the Proton/Electron Telescope (PET) (Cook et al., 1993) aboard the Solar Anomalous Magnetospheric Particle Explorer (SAMPEX) spacecraft (Baker et al., 1993), sampled at 6-s resolution. SAMPEX was a low Earth-orbiting spacecraft, its altitude varying over 450–700 km, decreasing over the course of the mission lifetime. The orbit had an 82° inclination and approximately 90-min period. SAMPEX was operational from 1992 to 2012 and calibrated PET data are available from July 1992 to June 2004.

We use the low energy electron channel (ELO). In the instrument paper (Cook et al., 1993), this channel is described as having an energy range of 1.5–6.0 MeV. However, Selesnick (2015) demonstrated that the energy ranges specified may not always be accurate and that PET was susceptible to contamination from protons when SAMPEX was passing through the inner belt, and to particles with energies as low as 0.63 MeV when passing through the outer belt during heightened periods of activity. Since we are analyzing active periods, we consider it likely that PET was measuring particles >0.63 MeV. This will not impact the overarching conclusions of the analysis in this study, as we are still analyzing relativistic or near-relativistic particles over a wide energy range.

2.1. L^* and Pitch Angle Sensitivity

As mentioned previously, Roederer's L^* parameter is the radial distance in a dipole field that encompasses the same amount of flux encircled by a drifting particle (Roederer, 1967). It essentially allows us to label the

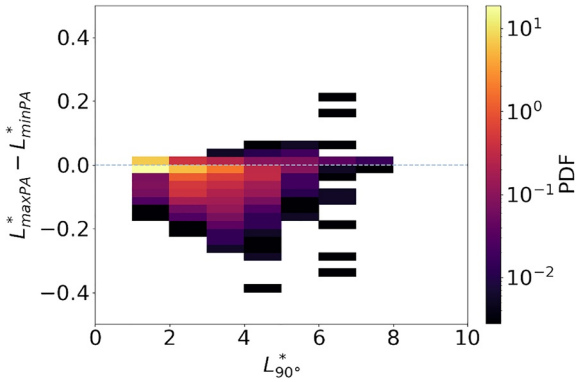

Figure 1. The probability density function (PDF) of variations in L* ($L^*_{maxPA} - L^*_{minPA}$) as the 90° L^* increases. The horizontal dashed line represents where there would be no variation.

drift path of a trapped particle, as an alternative to the dipole-like approximation of the IGRF L-shell parameter. We calculate L* using the IRBEM library (Boscher et al., 2010) and the Tsyganenko and Sitnov (2005) magnetic field model to replace L-shell in the SAMPEX data. This essentially simulates a full drift path of a particle with a given pitch angle (in this case 90°), independently of energy. To produce a cross-L* correlation matrix, we bin electron flux by L*. However, L* varies with pitch angle and given that PET had a large angular acceptance, we examine how this may influence the L* calculation.

For each 6-s sample from October and November 2003 we calculate three L* values for the location of SAMPEX; one for particles with a pitch angle of 90° at the satellite ($L^*_{90°}$), one for the minimum observed pitch angle (L^*_{minPA}), and one for a maximum observed (L^*_{maxPA}) pitch angle. Note that both hemispheres are considered, that is, all pitch angles between 0° and 180°. Minimum and maximum pitch angles are determined by the minimum and maximum pitch angle viewed by PET for which an L* can be returned. If the pitch angle at the edge of the PET field of view is within either the bounce or drift loss cone such that no L* value is returned, the pitch angle input is varied within the range observed by PET until a value is returned. The local $L^*_{90°}$ is calculated whether it is within the PET field of view or not. $L^*_{maxPA} - L^*_{minPA}$ is found for each sample and the probability density function (PDF) is plotted for the respective $L^*_{90°}$ in 1 L^* bins, shown in Figure 1. This shows how much L* generally varies with respect to $L^*_{90°}$. As the values here are calculated during the most geomagnetically active period in the entire SAMPEX data set, we expect this to show the widest range and be representative of the range of L* observed by SAMPEX over the entire 12-year of available data. Many of the variations are ≈0 and the overwhelming majority of variations are within 0.2 L^*. We will therefore bin the electron fluxes in bins of 0.2 L* in order to capture all possible L* variation within a single bin, removing any impact on our analysis.

2.2. Observed Flux Populations

Since the calculation of L* is obtained by simulating an entire particle drift path, L* can only be calculated for stably trapped electrons (where electrons can complete a full azimuthal drift path without being lost, and hence remain trapped indefinitely). Consequently, the L* calculation provides an accurate identification of when and where SAMPEX was within the stable trapping region. Since we calculate L* for particles with 90°pitch angles, we restrict the data to when part of the PET field of view was perpendicular to the magnetic field. This ensures that we are using the correct L* for the observed particles, regardless of the attitude configuration of the spacecraft.

Figure 2 shows the occurrence rate of of observations of the trapped electrons by PET in 1° × 1° bins in geodetic coordinates for the year 2003. Note that whether or not PET observed trapped particles is dependent on both the magnetic field model and the look direction of the instrument, which varied with time. We note that due to the wide 58° field of view of PET, the measurements may also include un-trapped particles (particles in the bounce or drift loss cones). However, in our analysis (described in more detail in Section 2.3) we use the maximum flux observed at a given L* during a 12-hr window, which means that the impact of PET observing a proportion of un-trapped particles can be assumed negligible. Figure 2 shows that trapped particles can only be viewed by PET when it was in and around the South Atlantic Anomaly region. It is unsurprising due to the 600 km altitude of SAMPEX, that PET spends most of the time observing inside either the bounce and/or drift loss cone (BLC and/or DLC), but the significance of the trapped flux observations allows for viable analysis of trapped electrons. This is also in agreement with other studies, which attempt to distinguish individual particle populations with low altitude spacecraft (Dietrich et al., 2010; Rodger, Carson, et al., 2010; Rodger, Clilverd, et al., 2010; Rodger et al., 2013; Selesnick, 2015) including the SAMPEX HILT instrument (Klecker et al., 1993).

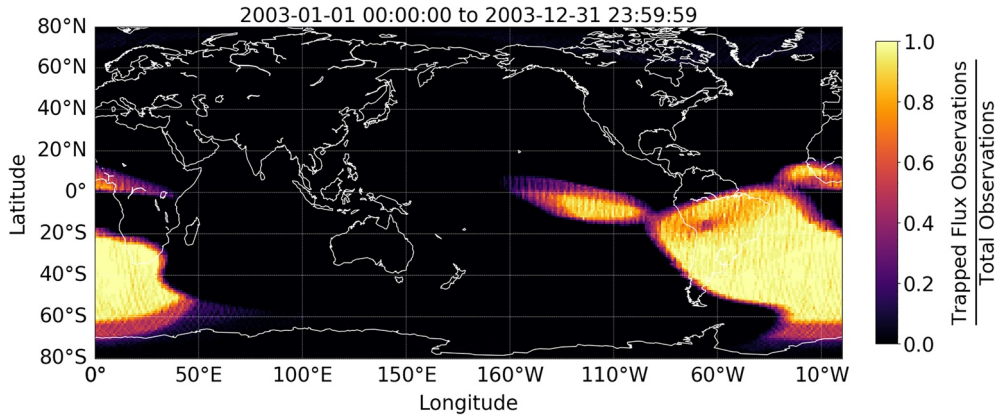

Figure 2. A world map in geodetic coordinates, showing where Proton/Electron Telescope (PET) generally observed trapped flux during the year 2003. Latitude-longitude bins are 1° × 1° in size, each containing the ratio of the number of occurrences where PET observed trapped flux, to the total number of occurrences.

2.3. Correlation Matrices

To analyze the cross-L^* coherence of the PET electron flux, we produce a series of correlation matrices, which show the correlation of flux at a given L^* with flux at every other L^*. Figure 3 shows a step-by-step example of how the matrices are produced, using 10th-30th November 2003, during which was the November 2003 Hallowe'en storm. Figure 3a shows the PET electron flux between $L^* = 2.0 - 6.6$ binned in 0.2 L^*

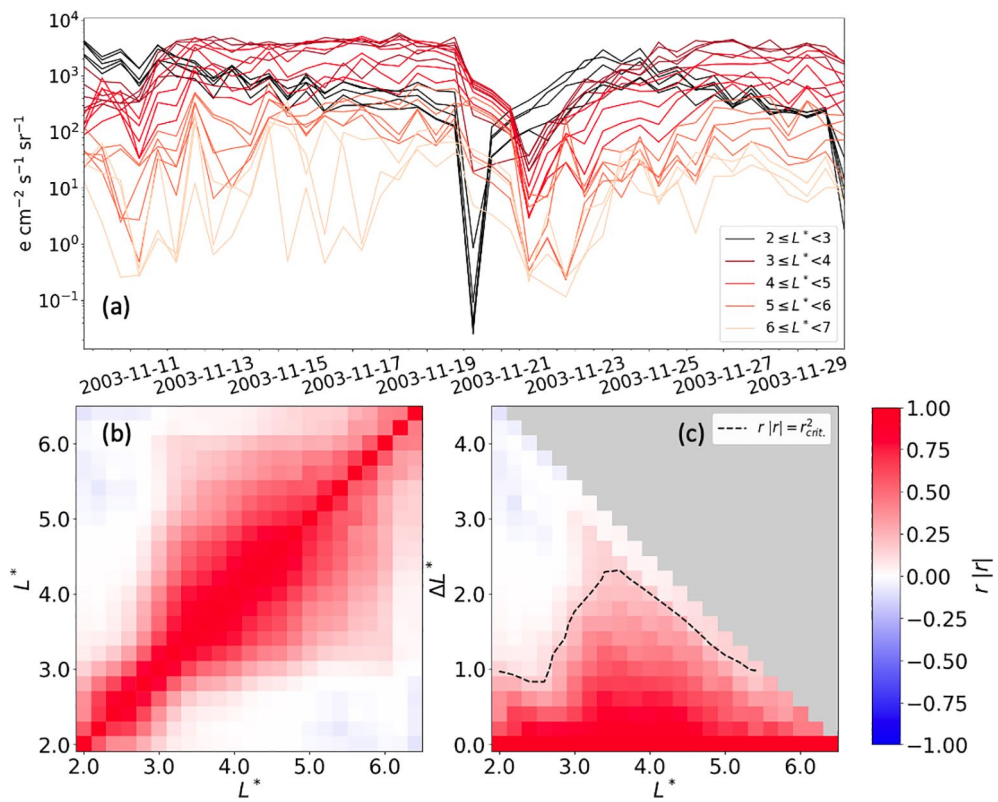

Figure 3. (a) A selection of L^*-binned >0.63 MeV fluxes observed by Proton/Electron Telescope from 10th to 30th November 2003, at 12-hr resolution. (b) The resulting L^* versus L^* correlation matrix from the same dates. (c) The ΔL^* versus L^* correlation matrix, adapted from (b). The color shows $r|r|$, derived from the Pearson's correlation coefficient. Gray represents a bin containing no data. The black, dashed contour indicates where $r|r| = r^2_{crit.}$, the threshold at which we reject the null hypothesis that $r|r| = 0$ at the 99% confidence level.

intervals, as this was the maximum L^* range which provided sufficient coverage required for the analysis. Flux is sampled in 12-hr time intervals to remove periodic 12-hr flux variations caused by the Earth's rotation, periodically subjecting PET to the SAA. We take the maximum value per 12-hr rather than the mean, as this naturally maximizes the portion of trapped particles in the PET field of view due to their high intensity. Each line in Figure 3a shows the electron flux in a different L^* bin, with the line colors indicating a range of L^*. Pearson's correlation coefficient is then calculated for every combination of L^* bins, and plotted on an L^* versus L^* matrix shown in Figure 3b. The coefficients used in the matrix are the Pearson's correlation coefficient (r) multiplied by its own magnitude ($|r|$), or $r|r|$. Similar to r^2, $r|r|$ shows the proportion of the variability in one time series that is related to the variability in the other, but also indicates whether the variations are in or out of phase. By design, the matrix in Figure 3b is symmetric about the the $L^*_x = L^*_y$ line. We therefore transform the coordinates of Figure 3b such that the $L^*_x = L^*_y$ lies along the X-axis as in Figure 3c. Figure 3c is thus a ΔL^* versus L^* matrix, where ΔL^* refers to the distance in L^*, outwards from its corresponding L^* value. Figure 3c is the style of plot that will now be referred to as a "correlation matrix." In order to add confidence to the coefficients in the correlation matrices, we complete a null hypothesis test using the Student's t-distribution (Student, 1908). Rather than calculating the t-statistic to obtain a p-value for each coefficient, we calculate the critical r^2 value ($r^2_{crit.}$) for the 99% confidence level. This allows us to reject the null hypothesis that $r|r| = 0$ where $r|r| \geq r^2_{crit.}$. The black, dashed contour line in Figure 3c indicates where $r|r| = r^2_{crit.}$.

Between 10 and 30 November 2003 there are two identifiable regions of positive (red) correlation: an inner region between $L^* = 2.0-3.0$ and an outer region between around $L^* = 3.0-5.5$. Flux at $L^* = 2.0$ is well correlated with flux up to $\Delta L^* \approx 1.0$ (i.e., flux at $L^* = 2.0$ with flux at $L^* \approx 3.0$) but does not correlate with flux at higher ΔL^* values. The limiting of the correlation of electron flux within the inner region is demonstrated by the triangular shape of the region of high correlation, since the ΔL^* over which the correlation is high reduces as $L^* = 3.0$ is approached. Correlation is strong within this region, with $|E$ values generally between 0.75 and 1.0, and declining outside the $L^* = 3.0$. Hence, flux variations within this region do not positively correlate with those where $L^* > 3.0$. This is clear in Figure 3a, as the $L^* = 2.0-3.0$ fluxes (black) simultaneously vary differently to flux at all other L^*. Using the same logic, we identify an outer region in which the flux variations are also strongly coherent between $L^* = 3.0-5.5$, before correlation begins to decline again. There is a small amount of positive correlation between the two regions ($L^* \approx 3.0$) which correlates with flux within $\Delta L^* \approx 0.5$. This cannot be considered a region of its own, because correlation within $\Delta L^* \approx 0.2$ is within the same bin, and so perfect correlation is to be expected. Also, flux within adjacent L^* bins may be subject to very localized processes, so could be expected to behave similarly within the immediately surrounding bins. It is also clear that correlation drops off with regions sharply outside $\Delta L^* \approx 0.5$ from $L^* = 3.0$ and remains close to zero thereon outwards. Figure 3 is also across a 20-day time period, where significant variation and differences in coherence are expected, which could blur any boundaries in this initial analysis. We note that although we have only examined fluxes at $L^* < 6.6$, the drop in correlation beyond $L^* = 5.5$ and the triangular shape of this outer region in Figure 3 is not a result of the upper limit of our analysis. Overall, we find that these correlation matrices can be a useful tool in identifying different regions in which the behavior of the electron flux was similar over periods of many days.

2.4. November 10–30, 2003 Case Study

In the above, we applied our correlation matrices analysis to a 20-day period encompassing periods of storm activity and non-storm times in between. In the following, we use the same 10–30 November time period to examine how the correlation between electron fluxes at different L^* varies on shorter time-scales and directly compare them. As explained above, our analysis is limited to a 12-hr sampling rate for PET data due to the significant periodic variation in flux measurements at higher resolution. We therefore limit the length of the analysis windows to 5-day (≈10 data points), as smaller lengths of time do not provide enough data to produce statistically significant results. We define four time periods of focus, relative to the minimum Sym-H time, T_0; "$T_{-10,-5}$," "$T_{-5,0}$," "$T_{0,5}$," and "$T_{5,10}$," where the subscript refers to the specific time period in days relative to minimum Sym-H (e.g., $T_{-10,-5}$ indicates the 5-day time period from 10 to 5 days prior). The minimum Sym-H time is obtained from an algorithm-generated storm list (Walach & Grocott, 2019). The case study is therefore a 20-day period centered on the time of minimum Sym-H, using 12-hr resolved data.

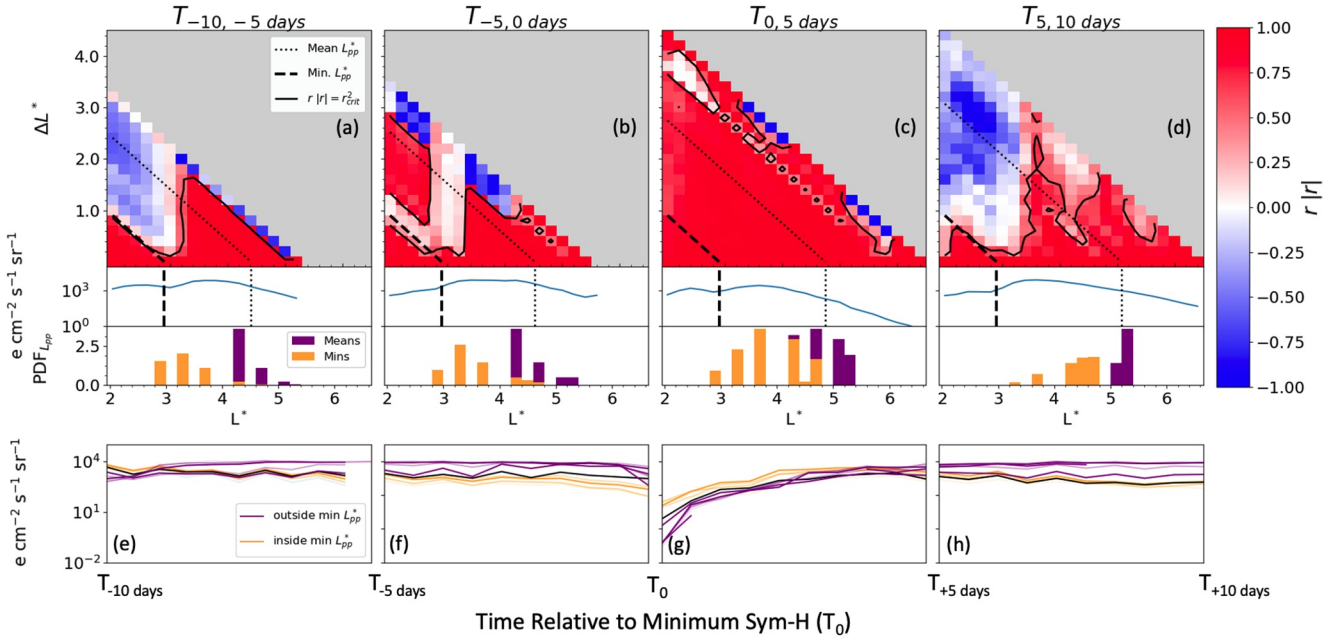

Figure 4. Case study of the November 2003 storm, defined relative to minimum Sym/H (T_0) on 2003-11-20 at 18:17:00. (a) $T_{-10,-5}$, or the period between 10 ($T_{-10days}$) and 5 days (T_{-5days}) before T_0. (b) $T_{-5,0}$ or between T_{-5days} and T_0. (c) $T_{0,5}$ or from T_0 to T_{+5days}. (d) $T_{5,10}$ or from T_{+5days} to $T_{+10days}$. The top panel of each is the correlation matrix for $L^* = 2.0 - 6.6$, with a contour at $r\,|r| = r^2_{crit.}$. The middle panel is the mean flux profile for the same L^* range and period and the bottom panel is the probability distribution function (PDF) of the minimum (orange) and mean (purple) model plasmapause locations for the time period, in L^* coordinates (L^*_{pp}). The dashed line is the minimum plasmapause location and the dotted line is the mean plasmapause location for that time period. (e–) show time series of each L^*-binned electron flux. The orange lines represent flux inside the minimum model plasmapause, and the purple outside. The transparency of the lines increases with increasing distance from the minimum plasmapause location.

The November 2003 Hallowe'en storm was the largest geomagnetic storm in solar cycle 23, reaching a minimum Sym-H of −490 nT, and has been extensively studied (e.g., Baker, Kanekal, Li, et al., 2004; Bortnik et al., 2006; De Franceschi et al., 2008; Horne, Thorne, Shprits, et al., 2005; Loto'aniu et al., 2006; Yahnina & Yahnin, 2014). It is notable for the fact that significant levels of electrons were observed within the slot region and inner belt, with high fluxes seen in there for weeks following the storm. The high fluxes in this region were also present before the storm as a result of the earlier October 2003 storm. Figures 4a–4d present data from the $T_{-10,-5}$, $T_{-5,0}$, $T_{0,5}$, and $T_{5,10}$ time periods respectively, associated with the 2003 Hallowe'en storm. The top panels show the corresponding correlation matrices, with an $r\,|r| = r^2_{crit.}$ contour over-plotted. The middle panels show the radial profile of the mean flux for each phase. The results from our analysis for $T_{-10,-5}$ show similarities with those shown in Figure 3: two regions ($L^* = 2.0 - 3.0$ and $L^* = 3.5 - 5.0$) within which the fluxes are significantly correlated, with correlations of $r\,|r| \geq 0.8$ within those regions. However, unlike the 20-day interval examined above, the fluxes inside $L^* = 3.0$ show an anti-correlation ($r\,|r| = -0.25$ to -0.5, colored blue) with fluxes outside $L^* = 3.0$.

The significance of $L^* = 3.0$ may be associated with the location of the plasmapause, but the plasmapause location varies significantly with MLT and AE. The bottom panels of Figure 4 therefore show the distribution of various measures of the (Meredith et al., 2018) model plasmapause locations using AE. Note that all model plasmapause locations are in L^* coordinates (denoted by L^*_{pp}) generated using the Olson and Pfitzer (1977) model. Despite the use of different model magnetic fields for the L^*_{pp} and L^*, the difference between the two is negligible at low L^* values (<4), thus the plasmasphere model can be applied in our L^* regime. For each 5-day time window, purple shows the distribution of L^*_{pp} averaged over MLT, and the black dotted line shows the mean of this distribution. Orange shows the distribution of the minimum L^*_{pp} for each timestamp. The black dashed line shows the minimum extent of this distribution. It is important to note that the black dashed line is not an averaged value (and hence contains no averaging uncertainties), but the absolute minimum L^*_{pp} at anytime during the respective time period. That is, locations inside this L^*_{pp} value will have remained inside the plasmapause the whole time, whereas locations outside the minimum but

inside the mean L^*_{pp} may have been outside the plasmapause for some of the time. Meredith et al. (2018) determined the plasmapause by fitting Gaussian profiles to a database of hiss and chorus emissions and taking the intersection point between the two. A statistical wave model-determined plasmapause is particularly useful because changes in electron behavior either side could potentially be attributed to these waves, however it should be noted that during most extreme events such as the main and early recovery phase of November 2003, the model may be less reliable. For example, the measurements presented in Baker, Kanekal, Li, et al. (2004) show that the plasmapause may have been inside $L^* = 2.0$ at points during the November 2003 storm.

Figures 4e–4h show the L^*-binned electron flux (as per Figure 3a) for the duration of the case study. Orange lines represent flux inside the minimum plasmapause, and purple lines outside. The transparency of the lines increase with increasing distance from the minimum plasmapause location. The single black line on each is flux in the same L^* bin as the minimum plasmapause. Figure 4e, suggests that this is a result of the fluxes inside of the minimum plasmapause location generally decreasing over the 5-day interval and vice-versa outside the minimum plasmapause. Figure 4e and the radial average flux profiles show that these correlations are derived when flux is present rather than due to a continuous lack of flux. Comparing the correlation matrix with the distributions of the model plasmapause locations, we find that the inner region of strong correlation falls within the minimum plasmapause location. The outer edge of the outer region does not appear to correspond to the other measures of the model plasmapause, but we note that our calculation of L^* does not return any values beyond $L^* = 5.3$ during this interval. The lack of an L^* value could attribute to the compressed magnetopause following the previous October storm, thus decreasing the extent of the outermost drift paths.

During $T_{-5,0}$ shown in Figures 4b and 4f, flux variations between $L^* = 2.0$–3.0 and between $L^* = 3.4-5.0$ are strongly correlated again, with $r|r| \geq 0.8$. However, unlike $T_{-10,-5}$, flux inside $L^* = 2.0$–3.0 now shows a strong positive correlation with flux at $L^* \geq 3.4$. Figure 4f shows that this may be due to most fluxes inside and outside minimum L^*_{pp} maintaining intensity rather than increasing, then sharply decreasing in the day before T_0. Interestingly, the correlation of fluxes close to L^*_{pp} drops to near-zero with all other fluxes. The features described could also be attributed to the mix of storm phases within our pre-defined 5-day time period. In Figure 4f, the main phase of the storm does not appear to begin until the final day of $T_{-5,0}$, signified by the sudden and rapid decrease in flux. The full extent of this loss is apparent at the beginning of $T_{0,5}$. For the first ≈4 days of $T_{-5,0}$ however, there is largely a continuation of the behavior from $T_{-10,-5}$, that being a gradually increasing or maintenance of flux outside the minimum plasmapause location and a gradual decrease inside. This suggests that an analysis of the main phase alone may find coherence across all L^*, regardless of the plasmapause. This also suggests that the initial phase may be more akin to $T_{-10,-5}$ or entirely different, though as explained, such a study is not possible with SAMPEX due to the time resolution constraints.

Figures 4c and 4g show data from $T_{0,5}$, a majority of which is during the storm recovery phase. Flux at virtually all L^* showed strong positive correlation in excess of $r|r| = 0.8$, regardless of the plasmapause location, indicating coherent changes across the whole outer radiation belt. Between the final point of Figure 4f and the first in Figure 4g (across T_0) there was a sharp decrease of flux at all L^* (a likely indication of the main phase). The subsequent increase of fluxes across all L^* in Figure 4g is a clear demonstration of overall coherence during the recovery phase in the days following minimum Sym-H. Despite the widespread coherence, the fluxes inside the plasmapause appear to increase with a slightly shallower gradient than of those outside and immediately begin decreasing again once peaked.

Data from $T_{5,10}$ is shown in Figures 4d and 4h. The $T_{5,10}$ correlation matrix shows some resemblance to that of $T_{-10,-5}$ and the 20-day average, with two regions of relatively strong coherence separated by the minimum plasmapause location for that time period. However, the correlation matrix shows much greater structure in the outer coherence region than seen during the others phases. As for previous periods, the flux between $L^* = 2.0-3.0$ was strongly coherent, with correlation coefficients of mainly $r|r| > 0.8$. Outside $L^* = 3.0$ the correlation matrix shows two regions. Correlation is strong between $L^* = 3.4 - 4.6$ and between $L^* = 4.6-6.0$, both with correlations coefficients of $r|r| > 0.8$. However, the two regions show a weaker ($r|r| < 0.8$) positive correlation with each other. We also note that the mean model plasmapause location lies between the two coherent outer regions. Figure 4h shows that flux outside the minimum plasmapause

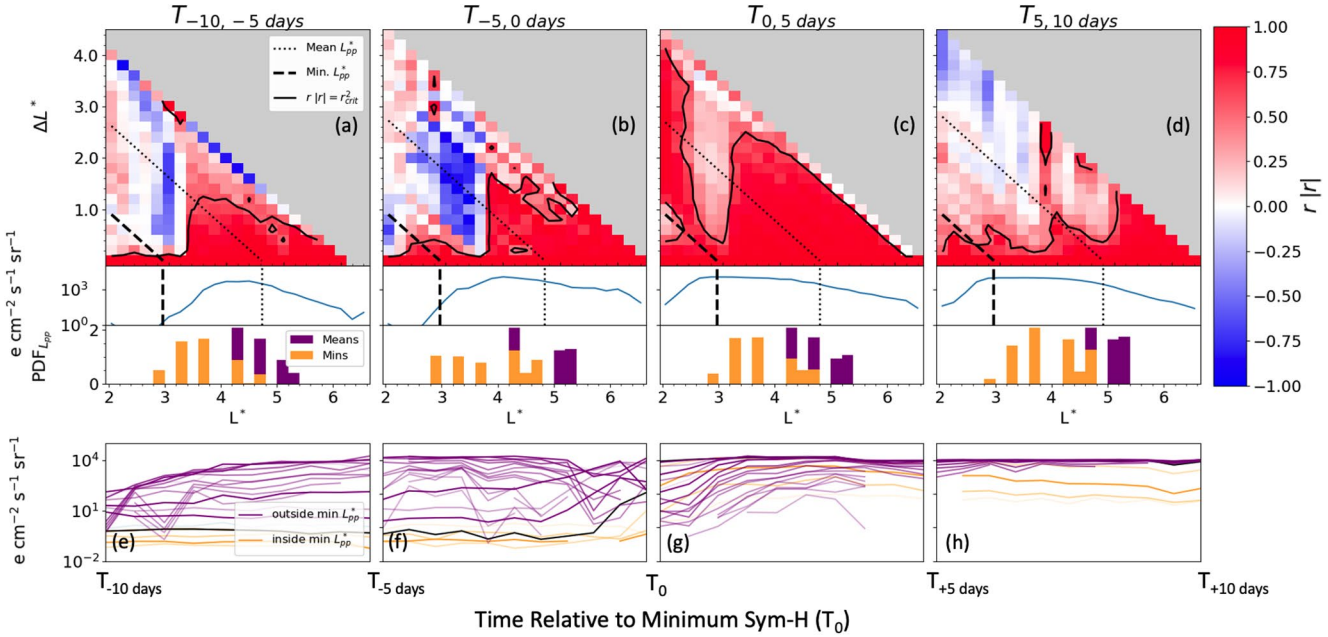

Figure 5. Case study of the May 2003 storm presented identically to that of Figure 4.

maintained its intensity during $T_{5,10}$, while flux inside gradually declined again. This is similar to $T_{-10,-5}$ and explains the two main regions of coherence, as well as the negative correlation between them.

In summary, we generally find two regions of coherence outside of the 5 days preceding of following minimum Sym-H, which becomes more coherent during the storm, more clearly the recovery phase. An inner region of coherence where the flux gradually decreases inside the minimum extent of the plasmapause, and an outer region where flux is maintained or gradually increases outside the minimum plasmapause location. Coherence is strong across all L^*, regardless of the plasmapause, during the 5 days following minimum Sym-H and thus the recovery phase. Similar behavior is also suggested during $T_{-5,0}$, possibly attributed to rapid loss during the main phase.

2.5. 24 April–14 May 1998 Case Study

As noted above, prior to the 2003 Hallowe'en storm, the fluxes between $L^* = 2.0-3.0$ were elevated due to an earlier event. During solar cycle 23, few events resulted in an injection into this region. We turn our attention now to an event where the $L^* = 2.0-3.0$ region initially has very low electron fluxes. In this section, we examine a relatively strong storm in May 1998 which reached Sym-H = −272 nT. The results of our analysis are shown in Figure 5.

Figures 5a and 5e show $T_{-10,-5}$. There is no strong correlation between flux variations inside $L^* = 2.0-3.2$, and this region does not strongly correlate with flux outside $L^* = 3.2$. The lack of correlation appears to be due to the low levels of flux inside $L^* = 3.2$ (≈minimum plasmapause) as shown by the mean radial profile and Figure 5e. Flux outside $L^* = 3.2$ was strongly correlating ($r\,|r| \geq 0.8$), though correlation decreased with increasing ΔL^*. Figure 5e shows that the strong correlation in the outer region is due to gradually increasing flux, much like the outer regions in Figure 4.

During $T_{-5,0}$ shown in Figures 5b and 5f, positive correlation within $L^* = 2.0-3.2$ strengthened, showing correlation coefficients of $r\,|r| > 0.25$ and in some areas $r\,|r| \geq 0.8$. The increased correlation could be a result of an increased flux between $L^* = 2.0 - 3.2$ as shown in the flux profile, though this is still relatively low and decreased quickly with decreasing L^*. The outer region of strong correlation did not begin until $L^* \approx 3.6$, and correlation coefficients of $r\,|r| > 0.8$ were not widespread until $L^* \approx 4.2$. The reduced overall correlation is also apparent in Figure 5f where flux outside the minimum plasmapause location varied by orders of magnitude. Flux inside the minimum plasmapause location was consistently low, but began to

increase within a day before T_0. As in Figure 4f, the sudden change in dynamics toward the end of $T_{-5,0}$ indicates the main phase coming into effect. Most of $T_{-5,0}$ is, again, a continuation of the dynamics seen in $T_{-10,-5}$. As already stated, we are unable to view timescales on the order of the main phase alone, due to the 12-hr resolution limit for this type of analysis with SAMPEX.

Figures 5c and 5g show the $T_{0,5}$, most of which again represents the recovery phase. The correlation matrix shows positive correlation across almost all L^*, regardless of the minimum plasmapause location. This is much like Figure 4c and is also due to the increasing of flux across all L^*, including that inside the minimum plasmapause as shown in Figure 5g. In this case however, correlation of flux close to the minimum plasmapause location is weaker with flux at all other L^*.

The $T_{5,10}$ correlation matrix (Figure 5d) shows overall less correlation than $T_{0,5}$. Flux within $L^* = 2.0-3.0$ (≈inside minimum plasmapause) is strongly correlated and did not correlate strongly with flux outside. This is shown by the gradual decrease of flux inside minimum plasmapause in Figure 5h. The inner region correlated weakly ($r|r| = -0.5$–0.5) with flux outside the minimum plasmapause. The positive correlation ends around $L^* = 5.0$, which is approximately the location of the overall mean plasmapause position. Correlation of flux inside mean L^*_{pp} correlates weakly and negatively with flux outside the mean plasmapause in this case. Figure 5h shows that the less-well structured outer region in $T_{5,10}$ is due to some of the flux maintaining a high intensity, and some still gradually increasing.

The November 2003 and May 1998 storms both indicate that the overall coherence of electron flux dynamics during periods of heightened activity was highly variable, but share some common features throughout. Notably, when flux was present minimum L^*_{pp}, there was a gradual and coherent reduction in intensity. Outside the minimum L^*_{pp}, flux varied between widespread coherence and generally coherent but with degrees of spatial variation. In any case, flux variations outside minimum L^*_{pp} were uncorrelated with flux inside the minimum L^*_{pp}. The $T_{0,5}$ period in both case studies (encompassing storm recovery phases) shows that flux variations were coherent across the entire range of interest due to the rapid recovery of fluxes at all L^*.

2.6. Statistical Analysis of Large Storms

We have shown that flux tends to coherently and gradually reduce when inside the minimum L^*_{pp} while behaving differently outside. To test the generality of the case study results, we identified 15 large storms (large referring to any storm reaching a minimum Sym-H below −200 nT, including the November 2003 and May 1998 events) between 1992 and 2004 from the Walach and Grocott (2019) list that were observed in their entirety by PET and analyzed them in the same way as the case studies above. Each corresponding correlation matrix for each of the previously defined time periods are then aligned at the minimum L^*_{pp} to calculate the mean correlation matrix. We align at the minimum L^*_{pp} because the case studies indicate that the minimum L^*_{pp} is the main focal point of differences in electron flux coherence. The x-axis of the mean correlation matrices therefore shows the difference in L^* from the minimum plasmapause location and the y-axis corresponds to the ΔL^* outward from the x-axis location. Figures 6a–6d show the mean correlation matrix for each time period on the top panel, and the bottom panel shows the mean radial profile with respect to the location of minimum L^*_{pp}, with the shaded region indicating standard deviation. Figures 6e–6h show the number of values in each bin of the corresponding correlation matrix. Most show the maximum of 15 values, however there is a gradient on the outer edge due to the alignment of all correlation matrices with minimum L^*_{pp}. The black dashed line on all panels refers to the minimum L^*_{pp}, to which all data is aligned.

Figure 6a shows the mean $T_{-10,-5}$ correlation matrix. Inside the minimum L^*_{pp}, correlation between flux was positive but weak on average, mainly between $r|r| = 0.0$–0.5. Fluxes inside the minimum plasmapause correlated weakly ($r|r| < 0.5$) with those outside the minimum L^*_{pp}. The radial profile of the mean flux (Figure 6a, bottom panel) shows that the average fluxes inside the minimum plasmapause were low and with a much larger standard deviation that at other L^*. This suggests that the lack of a strong correlation on average may be related to a lack of flux, as was the case during May 1998. Any storm where flux was present inside the minimum plasmapause and therefore coherent during pre-storm such as November 2003, would be countered by those where flux was not present and the correlations were low. Outside minimum L^*_{pp} flux showed overall positive correlation, mainly from $r|r| = 0.5$–1.0, and therefore were coherent during all or most of the storms. During $T_{-5,0}$ in Figure 6b, mean correlation slightly increased in strength from $T_{-10,-5}$ in-

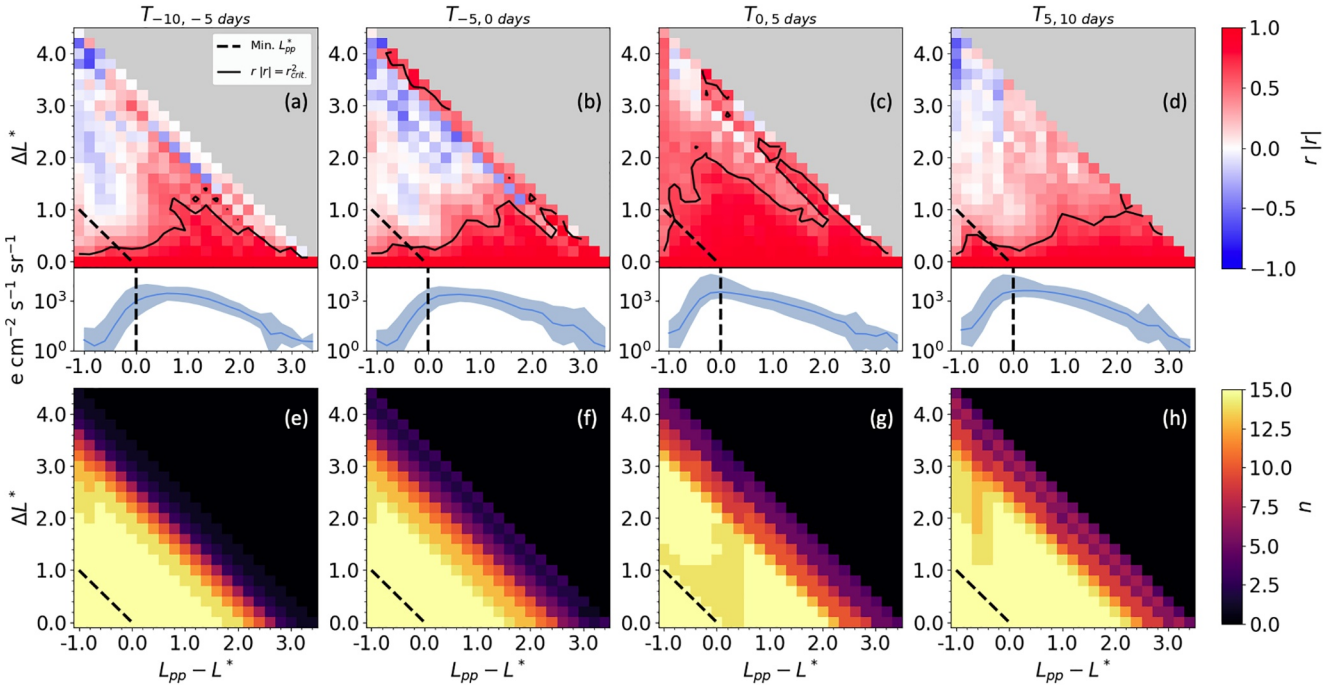

Figure 6. Statistical analysis of storms falling below −200 nT in Sym-H. (a–d) (Top panel) Mean correlation matrices for each time period, aligned at minimum L^*_{pp} with a contour at $r|r| = r^2_{crit.}$ for a single correlation matrix. (Bottom panel) Mean radial profile with respect to minimum L^*_{pp}, where the shaded region represents standard deviation. (e–h) The number of values in each bin of the above matrix. The *x*-axis describes location with respect to minimum L^*_{pp}, which is shown by the black dashed line in all panels.

side the minimum plasmapause. Flux outside the minimum plasmapause showed a reduction in overall correlation, particularly between flux of $\Delta L^* > 1.0$ separation, reducing below $r|r| \approx 0.6$. Correlation remained weak ($r|r| < 0.5$) between flux inside and outside minimum L^*_{pp}. $T_{0,5}$ for both November 2003 and May 1998 showed strongly coherent fluxes as a result of flux at all L^* rapidly increasing after minimum Sym-H. The mean $T_{0,5}$ (Figure 6c), which is also representative of the recovery phase, shows strong correlation across all L^*, with $r|r|$ values generally >0.6, regardless of minimum plasmapause location. This suggests that in all 15 storms, coherence during the recovery phase was due to a universal increase following a decrease during the final day of $T_{0,5}$. Correlation throughout $T_{5,10}$ in Figure 6d also reflects that of November 2003 and May 1998. The radial profile inside the minimum plasmapause increased in intensity following the rapid increase of all fluxes in $T_{0,5}$. This is visible in the mean $T_{5,10}$ correlation matrix as correlation strengthened inside the minimum plasmapause to >0.6. Flux outside the minimum plasmapause correlated again generally $r|r| > 0.6$, however, $T_{5,10}$ flux inside correlated weakly or negatively with flux outside. In both November 2003 and May 1998 this was also the case, due to fluxes maintaining or increasing to a high intensity outside the minimum plasmapause and flux inside gradually decreasing.

The statistical analysis of 15 large storms reinforces the key results of the November 2003 and May 1998 case studies. Flux variations are coherent inside minimum L^*_{pp} and outside, but do not correlate with each other. This suggests the behavior found in the case studies may also apply to other large events, where flux gradually reduced when inside minimum L^*_{pp} and either gradually increased or remained constant outside. Strong correlation across all L^* during the $T_{0,5}$ period is indicative of the rapid increase in flux at all L^* as also shown in the case studies. It is noted however, that correlation inside minimum L^*_{pp} is weaker in Figure 6 than in the case studies, likely due to the variation in the intensity of flux in this region between the 15 events. The variation inside minimum L^*_{pp} is apparent in the case studies, as the May 1998 event begins with much lower intensity in this region than the November 2003 event. This analysis suggests a clear plasmaspheric influence on the behavior of high energy electron flux in the outer radiation belt. Specifically, resulting in the constant gradual decrease of flux that permanently resides within the plasmasphere at all times except during the recovery phase of the storm. Although the influence of the plasmapause on MeV and near-MeV

electron flux variations have been studied previously, (e.g., Darrouzet et al., 2013; Hardman et al., 2015; Li et al., 2006; Lichtenberger et al., 2013; Whittaker et al., 2014) our analysis provides further evidence of these dynamics from perspective of radiation belt coherence, in a more detailed manner than before.

3. Discussion

In this study we analyze the storm time cross-L^* coherence of electrons in the outer radiation belt between $L^* = 2.0 - 6.6$ using correlation matrices. Case studies of storms in May 1998 and the 2003 Hallowe'en storm showed that more than 5-day preceding or following minimum Sym-H, the variations in the >0.63 MeV electron flux measured by SAMPEX were largely coherent inside of the minimum plasmapause location, although this coherence is limited when the fluxes are low. Fluxes outside the minimum plasmapause location were also coherent, but generally behave differently to those inside the minimum plasmapause. During the days following minimum Sym-H, mainly representative of storm recovery phases based on the storm times used, all the fluxes varied coherently, showing an increase at most L^*. The $T_{-5,0}$ periods of both case studies showed a less clear structure. The flux versus time plots in Figures 4 and 5 suggest that this is due to the effects of the main phases of each storm affecting the fluxes toward the end of the 5-day period. For the storm phase times (generated by the Walach & Grocott, 2019 algorithm) used in this analysis, it is indeed the case that the vast majority of main phase times occur within one day prior to the minimum Sym-H time. The effects in question resulted in the rapid loss of flux at most L^*, however flux inside the minimum plasmapause during the May 1998 case study began to increase instead. This may be related to the fact that flux was already very low during this time. Before the main phase but still during the 5-day $T_{-5,0}$ period, the results largely show a continuation of the behaviors seen in the 5-day pre-storm phase.

The statistical analysis of the 15 largest storms (in terms of Sym-H) observed fully by the SAMPEX PET instrument found similar results. All three analyses show agreement on the coherence of flux outside the minimum L^*_{pp}. When flux is present inside minimum L^*_{pp} it is also coherent, but uncorrelated with flux outside. This suggests the plasmasphere has a strong influence on the changes in electron flux intensity at most times, except during storm recovery phases and possibly the main phase.

The coherence of the variations in electron flux within the outer radiation belts has previously been examined by comparing fluxes at different altitudes and fluxes and different energies and pitch angles. Baker et al. (2001) compared flux measurements at high and low altitudes using data from SAMPEX and Polar respectively, finding similar flux variations at both altitudes. Kanekal et al. (2001) showed that flux at different altitudes on the same L-shell was also coherent by comparing observations from SAMPEX, Polar, GOES, and HEO, though with up-to 1 day of time lag. Chen et al. (2016) demonstrated cross-energy and cross-pitch-angle coherence by comparing electron flux from POES and Van Allen Probes spacecrafts, measuring $\approx keV$ flux in the loss cone and ≈MeV trapped flux respectively.

Vassiliadis et al. (2003) previously used the correlation technique we used but over a much longer 8-year period. Their results show clear regions of coherent flux variations: the slot ("S") region between $L = 2$–3, P_0, P_1 regions between $L = 3$–4 and 4–8 respectively, containing the majority of outer belt electrons, and P_2 region between $L = 8$–10, which is outside of our analysis range. The S region in Vassiliadis et al. (2003) differs from that seen in our analysis. This is likely due to the higher occurrence of slot-filling events in our data due to the focus on more active time periods. The mentioned study covers 8 years, within which there is a low occurrence of high flux intensity inside $L = 3.0$. The highly correlating $L > 3.0$ region commonly observed in our analysis occupies the same L-range as the P_0 and P_1 regions. Although we have not commonly observed the distinctive P_0 and P_1 regions, Figures 4d and 5d hint at this trend. Work in Vassiliadis et al. (2002, 2003, 2004, 2005); Vassiliadis (2008) suggests that these regions are also distinguished by the lag time in relation to solar wind velocity and others, with P_0 typically reacting sooner. While we cannot suggest this here, future work could apply the cross-correlation technique to compare with the claims of the mentioned studies, but specific to highly active times. The appearance of P_0 and P_1 during our $T_{5,10}$ periods does suggest however, that the mechanism may be dominated by other processes close to storm time or during extreme conditions which are not detectable in a longer-term study. It must also be noted that we use 12-hr resolution as opposed to daily resolution, which increases variability. Further, a longer study like the ones mentioned contain much smaller variability relative to the entire time window, allowing for longer-term

trends to be shown more clearly, whereas in our 5-day analyses, smaller and more localized variations could begin to dominate the correlation calculations.

Figures 4 and 5e–5h shed light on the reason that the coherence of changes in flux varies inside and outside the minimum plasmapause. During all non-storm times, the fluxes were generally high and maintained their intensity, or gradually increased outside the minimum plasmapause location. In contrast, the fluxes inside the minimum plasmapause location tended to decrease. Figures 4g and 4h show that even during highly coherent $T_{0,5}$ periods, fluxes inside the minimum L^*_{pp} increased with a shallower gradient and once peaked, immediately began slowly decreasing again. Fluxes outside the minimum plasmapause increase faster and then remain constant or gradually increase from there, causing the divergence between the two regions again and hence, the differing coherence during $T_{5,10}$. The relatively empty $T_{-10,-5}$ slot region of Figure 5 in May 1998 is an obvious difference between the two case studies, however, $T_{0,5}$ still shows flux at all L^* coherently increase, followed in $T_{5,10}$ by the maintenance of high fluxes outside the minimum plasmapause and gradual decrease of fluxes inside. This effect during the November 2003 Hallowe'en storm is also observed in Baker et al. (2007); Meredith et al. (2009), where the difference in loss timescales between low and high L is also apparent.

Kanekal et al. (2001) suggested that global coherence over less than 1-day timescales was evidence that acceleration processes are global in nature, acting across the magnetosphere. While over the examined 1-year period global processes may be more prominent, periods of heightened activity such as during a storm only make up a small portion of that, so may not show the effects of local acceleration. The 12-hr resolution used in this study is unlikely to directly capture local acceleration, but radial diffusion as a result of a local acceleration event (Ozeke et al., 2014) could be identified on this timescale. Moreover, our analysis is unable to discern inward and outward radial diffusion, so while the coherence shown may be inward radial diffusion on a global scale as with Kanekal et al. (2001), we cannot discount the effects of local acceleration driven by whistler-mode chorus waves.

Inside the minimum plasmapause location, our analysis generally shows strongly coherent flux variations which also behave differently to flux outside the minimum plasmapause. This region is loss-dominated when flux is present, with the exception of the recovery phase where all flux rapidly increases. The Meredith et al. (2018) model fitted Gaussian profiles to a database of hiss and chorus emissions and roughly determined the plasmapause from the intersection point of the two distributions. So, the plasmapause in our analysis is effectively the boundary between two wave populations; hiss inside the plasmapause and chorus outside. The minimum plasmapause is therefore the point at which flux inside is dominated by hiss waves, which are known to be effective at scattering electron pitch angles toward the loss cone (Abel & Thorne, 1998a, 1998b). Thus, it is likely that the region of coherent (and typically decreasing) flux inside the minimum plasmapause location is controlled by populations of hiss spanning multiple L^*.

During $T_{0,5}$ periods (recovery phases) where flux at all L^* is strongly coherent regardless of the plasmapause location, the affect of hiss is either severely weakened or insignificant compared to an energization process which increases flux at all L^*. Alternatively, the plasmapause could be close enough to the Earth such that it is inside the inner limit of $L^* = 2.0$ for the correlation matrices and all visible flux is actually outside the plasmapause, despite the model predictions and as is predicted by other physics-based models (Krall et al., 2017). However, the $T_{0,5}$ fluxes for, more visibly, November 2003 (Figure 4g) but also May 1998 (Figure 5g) show that during the rapid increase of all flux, that which is inside the minimum plasmapause location increases with a shallower gradient. Also, when the peak of flux inside the minimum plasmapause location is reached, the gradual decrease immediately follows and continues beyond the post-storm phase. This suggests that loss due to hiss wave scattering may still be present during the recovery phase, but the acceleration mechanism that provides increases in flux across all L^* is strong enough to dominate.

Murphy et al. (2018) analyzed the global response of the outer belt to geomagnetic storms, performing a superposed epoch analysis of various parameters during 73 storms. One of those parameters is the TRBEC index, where it is found that prior to minimum Sym-H, there is a mix of behavior, spanning from a small amount of loss to relatively constant. This behavior can also describe our statistical analysis of flux prior to minimum Sym-H. Here, we shed light on the spatial perspective as well as the net change. Due to the mix of storms beginning with pre-filled slot regions and empty slot regions, the analysis may be capturing a mix of

different responses to activity. With our case study of the November 2003 storm (Figure 4), the slot is already filled, and during the day or so before minimum Sym-H, flux at all L^* decreased and therefore constitutes a clear net loss. Our May 1998 case study (Figure 5) begins with an empty slot region at energies observed by PET. Not all fluxes outside the minimum plasmapause decrease, and those that do decrease, do so to a lesser extent to those during November 2003. This would therefore constitute a much more subtle net loss. It is reasonable therefore to infer that the unclear statistical results in here and Murphy et al. (2018) are due to differing initial conditions, as well as differing behavior in response to activity. Following minimum Sym-H Murphy et al. (2018) observes a more organized response, where in all storms there is a clear and consistent net increase of TRBEC. In all of our analyses, we observe a strongly coherent response in the recovery phase. Regardless of whether or not the slot region was filled prior to a storm, flux at all L^* coherently increased during the recovery phase and hence, the net increase in TRBEC. Murphy et al. (2020), using the RBC index (Baker, Kanekal, & Blake, 2004) also found net loss-dominated pre-minimum Sym-H (or Dst) and net enhancement-dominated recovery phase. The recovery phase being the only phase in which the entire belt was coherent also indicates that this is the only time during a storm when RBC and TRBEC are entirely representative, as they refer to net changes. Change in RBC or TRBEC suggests an overall coherent change in electron content, whereas outside of the recovery phase the reality would be a combination of two coherent areas, one of which is behaving differently to the other. The net changes in flux before and after storms in Reeves et al. (2003) may also hint at coherent changes which again, may not necessarily be the case.

For all of the above discussion, it is important to point out that our analysis contains a selection bias toward large storms. Future work will involve an analysis of a larger range of storms, including small and moderate, to determine whether our findings are reproduced in storms of any size. The slow precession and low altitude of the SAMPEX orbit means that we only see trapped populations for a limited time per day. Trapped flux can be multiple orders of magnitude more intense than flux in the loss cone and so for now, there is a 12-hr limit on the finest resolution of our analysis in order to avoid these patterns in the data dominating correlation coefficients. Five-day time windows were the lowest time window which could produce clear structure in our correlation matrices, and so we are limited to larger storms, which tend to last longer and fill some of the 5-day windows. If the temporal resolution of the flux measurements were improved, this would improve the resolution of our analysis and therefore allow more storms to be used, including smaller storms. We would also be able to consider exact storm phases in order to study the changes in coherence from the initial and main phase individually, as well as using exact times for the recovery phases. As shown in models such as Meredith et al. (2018), there is a much stronger presence of waves during storm times, differing hugely from that of quiet times. This presents clear opportunity to expand our analysis to quiet times in future work, comparing the coherence between quiet and active times.

4. Conclusions

We have used a correlation analysis to compare the coherence in L^* of the outer radiation belt. A selection of 15 large (≤200 nT in Sym-H) geomagnetic storms were broken down into four 5-day time periods surrounding the minimum Sym-H value of a storm. We provide two example case studies and finally a statistical analysis of all 15 storms. Our results show:

1. >0.63 MeV electron flux variations associated with storm time are coherent across L^* when outside the minimum plasmapause location.
2. Flux variations are coherent when inside the minimum plasmapause extent, but do not correlate with flux variations outside.
3. During storm main and recovery phases, flux variations across all L^* are coherent, irrespective of the plasmapause.

Our results show that fluxes inside the minimum plasmapause location (i.e., locations that are always within the plasmasphere) experience continual loss, except during the recovery phase of a storm. During the recovery phase, flux at all L^* regardless of the plasmapause location experiences a coherent net increase in flux, likely as a result of radial diffusion due to ULF or whistler-mode chorus waves, or local acceleration due to whistler-mode chorus. While we provide evidence that loss due to plasmaspheric hiss may still be

acting during this time, the recovery phase acceleration process (whose exact nature is unclear) is able to overcome it.

Data Availability Statement

Data from the SAMPEX PET instrument can freely be accessed at: http://www.srl.caltech.edu/sampex/DataCenter/data.html. AE data used to generate the model plasmapause can be found via OMNIWeb: https://spdf.gsfc.nasa.gov/pub/data/omni/high_res_omni/.

Acknowledgments
The authors would like to thank the many individuals involved in the operation of SAMPEX over 20 years. S. D. Walton was supported by Science and Technology Facilities Council (STFC) studentship NE/T014164/1. C. Forsyth was supported by NERC Independent Research Fellowship NE/N014480/1. C. Forsyth and I. J. Rae were supported by NERC Highlight Topic Grant NE/P017185/1 (Rad-Sat) and NERC SWIMMR Grant NE/V002554/1. C. E. J. Watt was supported by STFC grant ST/R000921/1 and NERC Rad-Sat Consortium grant NE/P017274/1. R. L. Thompson was supported by Engineering and Physical Sciences Research Council (EPSRC) grant EP/L016613/1. R. B. Horne, N. P. Meredith, and S. A. Glauert were supported by NERC Highlight Topic Grant NE/P01738X/1 (Rad-Sat) and NERC grant NE/V00249X/1 (Sat-Risk). M.-T. Walach was funded by NERC (Project codes NE/P001556/1 and NE/T000937/1).

References

Abel, B., & Thorne, R. M. (1998a). Electron scattering loss in Earth's inner magnetosphere: 1. Dominant physical processes. *Journal of Geophysical Research*, *103*(A2), 2385–2396. https://doi.org/10.1029/97ja02919

Abel, B., & Thorne, R. M. (1998b). Electron scattering loss in Earth's inner magnetosphere: 2. Sensitivity to model parameters. *Journal of Geophysical Research*, *103*(A2), 2397–2407. https://doi.org/10.1029/97ja02920

Albert, J. M., Selesnick, R. S., Morley, S. K., Henderson, M. G., & Kellerman, A. C. (2018). Calculation of last closed drift shells for the 2013 GEM radiation belt challenge events. *Journal of Geophysical Research: Space Physics*, *123*(11), 9597–9611. https://doi.org/10.1029/2018ja025991

Baker, D. N., Kanekal, S. G., & Blake, J. B. (2004). Characterizing the Earth's outer Van Allen zone using a radiation belt content index. *Space Weather*, *2*(2). https://doi.org/10.1029/2003sw000026

Baker, D. N., Kanekal, S. G., Blake, J. B., & Pulkkinen, T. I. (2001). The global efficiency of relativistic electron production in the Earth's magnetosphere. *Journal of Geophysical Research*, *106*(A9), 19169–19178. https://doi.org/10.1029/2000JA003023

Baker, D. N., Kanekal, S. G., Horne, R. B., Meredith, N. P., & Glauert, S. A. (2007). Low-altitude measurements of 2–6 MeV electron trapping lifetimes at $1.5 \leq L \leq 2.5$. *Geophysical Research Letters*, *34*(20), L20110. https://doi.org/10.1029/2007gl031007

Baker, D. N., Kanekal, S. G., Li, X., Monk, S. P., Goldstein, J., & Burch, J. L. (2004). An extreme distortion of the Van Allen belt arising from the 'Hallowe'en' solar storm in 2003. *Nature*, *432*(7019), 878–881. https://doi.org/10.1038/nature03116

Baker, D. N., Mason, G., Figueroa, O., Colon, G., Watzin, J., & Aleman, R. (1993). An overview of the Solar Anomalous, and Magnetospheric Particle Explorer (SAMPEX) mission. *IEEE Transactions on Geoscience and Remote Sensing*, *31*(3), 531–541. https://doi.org/10.1109/36.225519

Bortnik, J., Thorne, R. M., O'Brien, T. P., Green, J. C., Strangeway, R. J., Shprits, Y. Y., & Baker, D. N. (2006). Observation of two distinct, rapid loss mechanisms during the 20 November 2003 radiation belt dropout event. *Journal of Geophysical Research*, *111*(A12), A12216. https://doi.org/10.1029/2006ja011802

Boscher, D., Bourdarie, S., O'Brien, P., & Guild, T. (2010). IRBEM library V4.3. *Journal of Geophysical Research*. Retrieved from https://sourceforge.net/projects/irbem/

Boyd, A. (2016). *Quantifying the role of the seed population in radiation belt dynamics* (Doctoral Dissertations). Retrieved from https://scholars.unh.edu/dissertation/2245

Brito, T., Hudson, M. K., Kress, B., Paral, J., Halford, A., Millan, R., & Usanova, M. (2015). Simulation of ULF wave-modulated radiation belt electron precipitation during the 17 March 2013 storm. *Journal of Geophysical Research: Space Physics*, *120*(5), 3444–3461. https://doi.org/10.1002/2014ja020838

Carpenter, D. L. (1963). Whistler evidence of a 'knee' in the magnetospheric ionization density profile. *Journal of Geophysical Research*, *68*(6), 1675–1682. https://doi.org/10.1029/jz068i006p01675

Carpenter, D. L. (1966). Whistler studies of the plasmapause in the magnetosphere: 1. Temporal variations in the position of the knee and some evidence on plasma motions near the knee. *Journal of Geophysical Research*, *71*(3), 693–709. https://doi.org/10.1029/jz071i003p00693

Carpenter, D. L. (1978). New whistler evidence of a dynamo origin of electric fields in the quiet plasmasphere. *Journal of Geophysical Research*, *83*(A4), 1558. https://doi.org/10.1029/ja083ia04p01558

Chen, Y., Reeves, G. D., Cunningham, G. S., Redmon, R. J., & Henderson, M. G. (2016). Forecasting and remote sensing outer belt relativistic electrons from low Earth orbit. *Geophysical Research Letters*, *43*(3), 1031–1038. https://doi.org/10.1002/2015gl067481

Chen, Y., Reeves, G. D., Fu, X., & Henderson, M. (2019). PreMevE: New predictive model for megaelectron-volt electrons inside Earth's outer radiation belt. *Space Weather*, *17*(3), 438–454. https://doi.org/10.1029/2018sw002095

Claudepierre, S. G., & O'Brien, T. P. (2020). Specifying high-altitude electrons using low-altitude LEO systems: The SHELLS model. *Space Weather*, *18*(3). https://doi.org/10.1029/2019sw002402

Cook, W., Cummings, A., Cummings, J., Garrard, T., Kecman, B., Mewaldt, R., et al. (1993). PET: A proton/electron telescope for studies of magnetospheric, solar, and galactic particles. *IEEE Transactions on Geoscience and Remote Sensing*, *31*(3), 565–571. https://doi.org/10.1109/36.225523

Cosgrove, R., & Sanchez, E. (2012). Correlation as a global measure of geomagnetic activity: Phase boundaries and a precedent line of nodes. *Journal of Geophysical Research*, *117*(6), 6209. https://doi.org/10.1029/2011JA017483

Darrouzet, F., Pierrard, V., Benck, S., Lointier, G., Cabrera, J., Borremans, K., et al. (2013). Links between the plasmapause and the radiation belt boundaries as observed by the instruments CIS, RAPID, and WHISPER onboard Cluster. *Journal of Geophysical Research: Space Physics*, *118*(7), 4176–4188. https://doi.org/10.1002/jgra.50239

De Franceschi, G., Alfonsi, L., Romano, V., Aquino, M., Dodson, A., Mitchell, C. N., et al. (2008). Dynamics of high-latitude patches and associated small-scale irregularities during the October and November 2003 storms. *Journal of Atmospheric and Solar-Terrestrial Physics*, *70*(6), 879–888. https://doi.org/10.1016/j.jastp.2007.05.018

Dietrich, S., Rodger, C. J., Clilverd, M. A., Bortnik, J., & Raita, T. (2010). Relativistic microburst storm characteristics: Combined satellite and ground-based observations. *Journal of Geophysical Research*, *115*(A12). https://doi.org/10.1029/2010ja015777

Fermi, E. (1949). On the origin of the cosmic radiation. *Physical Review*, *75*(8), 1169–1174. https://doi.org/10.1103/PhysRev.75.1169

Friedel, R., Reeves, G., & Obara, T. (2002). Relativistic electron dynamics in the inner magnetosphere—A review. *Journal of Atmospheric and Solar-Terrestrial Physics*, *64*(2), 265–282. https://doi.org/10.1016/s1364-6826(01)00088-8

Goldstein, J., Sandel, B. R., Thomsen, M. F., Spasojević, M., & Reiff, P. H. (2004). Simultaneous remote sensing and in situ observations of plasmaspheric drainage plumes. *Journal of Geophysical Research*, *109*(A3). https://doi.org/10.1029/2003JA010281

Gringauz, K. I. (1963). The structure of the ionized gas envelope of earth from direct measurements in the U.S.S.R. of local charged particle concentrations. *Planetary and Space Science*, *11*(3), 281–296. https://doi.org/10.1016/0032-0633(63)90030-8

Hardman, R., Clilverd, M. A., Rodger, C. J., Brundell, J. B., Duthie, R., Holzworth, R. H., et al. (2015). A case study of electron precipitation fluxes due to plasmaspheric hiss. *Journal of Geophysical Research: Space Physics*, *120*(8), 6736–6748. https://doi.org/10.1002/2015ja021429

Horne, R. B., & Thorne, R. M. (1998). Potential waves for relativistic electron scattering and stochastic acceleration during magnetic storms. *Geophysical Research Letters*, *25*(15), 3011–3014. https://doi.org/10.1029/98GL01002 @ https://doi.org/10.1002/(ISSN)1944-8007.ISTPP1

Horne, R. B., Thorne, R. M., Glauert, S. A., Albert, J. M., Meredith, N. P., & Anderson, R. R. (2005). Timescale for radiation belt electron acceleration by whistler mode chorus waves. *Journal of Geophysical Research*, *110*(A3). https://doi.org/10.1029/2004JA010811

Horne, R. B., Thorne, R. M., Shprits, Y. Y., Meredith, N. P., Glauert, S. A., Smith, A. J., et al. (2005). Wave acceleration of electrons in the Van Allen radiation belts. *Nature*, *437*(7056), 227–230. https://doi.org/10.1038/nature03939

Hwang, J. A., Lee, D.-Y., Lyons, L. R., Smith, A. J., Zou, S., Min, K. W., et al. (2007). Statistical significance of association between whistler-mode chorus enhancements and enhanced convection periods during high-speed streams. *Journal of Geophysical Research*, *112*(A9). https://doi.org/10.1029/2007JA012388

Kanekal, S. G., Baker, D. N., & Blake, J. B. (2001). Multisatellite measurements of relativistic electrons: Global coherence. *Journal of Geophysical Research*, *106*(A12), 29721–29732. https://doi.org/10.1029/2001ja000070

Klecker, B., Hovestadt, D., Scholer, M., Arbinger, H., Ertl, M., Kastele, H., et al. (1993). HILT: A heavy ion large area proportional counter telescope for solar and anomalous cosmic rays. *IEEE Transactions on Geoscience and Remote Sensing*, *31*(3), 542–548. https://doi.org/10.1109/36.225520

Krall, J., Huba, J. D., & Sazykin, S. (2017). Erosion of the plasmasphere during a storm. *Journal of Geophysical Research: Space Physics*, *122*(9), 9320–9328. https://doi.org/10.1002/2017ja024450

Lejosne, S., & Kollmann, P. (2020). Radiation belt radial diffusion at Earth and beyond. *Space Science Reviews*, *16*(1). https://doi.org/10.1007/s11214-020-0642-6

Lemaire, J. F., Gringauz, K. I., Carpenter, D. L., & Bassolo, V. (1998). *The Earth's plasmasphere*. Cambridge University Press. https://doi.org/10.1017/CBO9780511600098.004

Li, X., Baker, D. N., O'Brien, T. P., Xie, L., & Zong, Q. G. (2006). Correlation between the inner edge of outer radiation belt electrons and the innermost plasmapause location. *Geophysical Research Letters*, *33*(14), L14107. https://doi.org/10.1029/2006gl026294

Lichtenberger, J., Clilverd, M. A., Heilig, B., Vellante, M., Manninen, J., Rodger, C. J., et al. (2013). The plasmasphere during a space weather event: First results from the PLASMON project. *Journal of Space Weather and Space Climate*, *3*, A23. https://doi.org/10.1051/swsc/2013045

Loto'aniu, T. M., Mann, I. R., Ozeke, L. G., Chan, A. A., Dent, Z. C., & Milling, D. K. (2006). Radial diffusion of relativistic electrons into the radiation belt slot region during the 2003 Halloween geomagnetic storms. *Journal of Geophysical Research*, *111*, 4218. https://doi.org/10.1029/2005JA011355

Lyons, L. R., Lee, D. Y., Thorne, R. M., Horne, R. B., & Smith, A. J. (2005). Solar wind-magnetosphere coupling leading to relativistic electron energization during high-speed streams. *Journal of Geophysical Research*, *110*(A11). https://doi.org/10.1029/2005JA011254

Lyons, L. R., & Thorne, R. M. (1973). Equilibrium structure of radiation belt electrons. *Journal of Geophysical Research*, *78*(13), 2142–2149. https://doi.org/10.1029/ja078i013p02142

Lyons, L. R., Thorne, R. M., & Kennel, C. F. (1972). Pitch-angle diffusion of radiation belt electrons within the plasmasphere. *Journal of Geophysical Research*, *77*(19), 3455–3474. https://doi.org/10.1029/ja077i019p03455

Mann, I. R., Ozeke, L. G., Morley, S. K., Murphy, K. R., Claudepierre, S. G., Turner, D. L., et al. (2018). Reply to 'The dynamics of Van Allen belts revisited'. *Nature Physics*, *14*(2), 103. https://doi.org/10.1038/nphys4351

Mann, I. R., Ozeke, L. G., Murphy, K. R., Claudepierre, S. G., Turner, D. L., Baker, D. N., et al. (2016). Explaining the dynamics of the ultra-relativistic third Van Allen radiation belt. *Nature Physics*, *12*(10), 978–983. https://doi.org/10.1038/nphys3799

Meredith, N. P., Horne, R. B., Glauert, S. A., & Anderson, R. R. (2007). Slot region electron loss timescales due to plasmaspheric hiss and lightning-generated whistlers. *Journal of Geophysical Research*, *112*(8). https://doi.org/10.1029/2007ja012413

Meredith, N. P., Home, R. B., Glauert, S. A., Baker, D. N., Kanekal, S. G., & Albert, J. M. (2009). Relativistic electron loss timescales in the slot region. *Journal of Geophysical Research*, *114*(3). https://doi.org/10.1029/2008JA013889

Meredith, N. P., Horne, R. B., Kersten, T., Li, W., Bortnik, J., Sicard, A., & Yearby, K. H. (2018). Global model of plasmaspheric hiss from multiple satellite observations. *Journal of Geophysical Research: Space Physics*, *123*(6), 4526–4541. https://doi.org/10.1029/2018JA025226

Meredith, N. P., Horne, R. B., Shen, X., Li, W., & Bortnik, J. (2020). Global model of whistler mode chorus in the near-equatorial region ($|\lambda m| < 18°$). *Geophysical Research Letters*, *47*(11). https://doi.org/10.1029/2020gl087311

Meredith, N. P., Horne, R. B., Thorne, R. M., Summers, D., & Anderson, R. R. (2004). Substorm dependence of plasmaspheric hiss. *Journal of Geophysical Research*, *109*(A6), A06209. https://doi.org/10.1029/2004ja010387

Millan, R., & Thorne, R. (2007). Review of radiation belt relativistic electron losses. *Journal of Atmospheric and Solar-Terrestrial Physics*, *69*(3), 362–377. https://doi.org/10.1016/j.jastp.2006.06.019

Murphy, K. R., Mann, I. R., Sibeck, D. G., Rae, I. J., Watt, C., Ozeke, L. G., et al. (2020). A framework for understanding and quantifying the loss and acceleration of relativistic electrons in the outer radiation belt during geomagnetic storms. *Space Weather*, *18*(5). https://doi.org/10.1029/2020sw002477

Murphy, K. R., Watt, C. E. J., Mann, I. R., Jonathan Rae, I., Sibeck, D. G., Boyd, A. J., et al. (2018). The global statistical response of the outer radiation belt during geomagnetic storms. *Geophysical Research Letters*, *45*(9), 3783–3792. https://doi.org/10.1002/2017gl076674

Olson, W. P., & Pfitzer, K. A. (1977). *Magnetospheric magnetic field modeling* (Annual scientific report). U.S. Department of Energy. Retrieved from https://www.osti.gov/biblio/7212748

Ozeke, L. G., Mann, I. R., Claudepierre, S. G., Henderson, M., Morley, S. K., Murphy, K. R., et al. (2019). The March 2015 superstorm revisited: Phase space density profiles and fast ULF wave diffusive transport. *Journal of Geophysical Research: Space Physics*, *124*(2), 1143–1156. https://doi.org/10.1029/2018ja026326

Ozeke, L. G., Mann, I. R., Murphy, K. R., Degeling, A. W., Claudepierre, S. G., & Spence, H. E. (2018). Explaining the apparent impenetrable barrier to ultra-relativistic electrons in the outer Van Allen belt. *Nature Communications*, *9*(1), 1844. https://doi.org/10.1038/s41467-018-04162-3

Ozeke, L. G., Mann, I. R., Murphy, K. R., Jonathan Rae, I., & Milling, D. K. (2014). Analytic expressions for ULF wave radiation belt radial diffusion coefficients. *Journal of Geophysical Research: Space Physics*, *119*(3), 1587–1605. https://doi.org/10.1002/2013JA019204

Ozeke, L. G., Mann, I. R., Olifer, L., Dufresne, K. Y., Morley, S. K., Claudepierre, S. G., et al. (2020). Rapid outer radiation belt flux dropouts and fast acceleration during the March 2015 and 2013 storms: The role of ultra-low frequency wave transport from a dynamic outer boundary. *Journal of Geophysical Research: Space Physics*, *125*(2). https://doi.org/10.1029/2019ja027179

Rae, I. J., Murphy, K. R., Watt, C. E., Halford, A. J., Mann, I. R., Ozeke, L. G., et al. (2018). The role of localized compressional ultra-low frequency waves in energetic electron precipitation. *Journal of Geophysical Research: Space Physics*, *123*(3), 1900–1914. https://doi.org/10.1002/2017JA024674

Reeves, G. D., McAdams, K. L., Friedel, R. H. W., & O'Brien, T. P. (2003). Acceleration and loss of relativistic electrons during geomagnetic storms. *Geophysical Research Letters*, *30*(10). https://doi.org/10.1029/2002gl016513

Rodger, C. J., Carson, B. R., Cummer, S. A., Gamble, R. J., Clilverd, M. A., Green, J. C., et al. (2010). Contrasting the efficiency of radiation belt losses caused by ducted and nonducted whistler-mode waves from ground-based transmitters. *Journal of Geophysical Research*, *115*(12). https://doi.org/10.1029/2010ja015880

Rodger, C. J., Clilverd, M. A., Green, J. C., & Lam, M. M. (2010). Use of POES SEM-2 observations to examine radiation belt dynamics and energetic electron precipitation into the atmosphere. *Journal of Geophysical Research*, *115*(A4). https://doi.org/10.1029/2008ja014023

Rodger, C. J., Kavanagh, A. J., Clilverd, M. A., & Marple, S. R. (2013). Comparison between POES energetic electron precipitation observations and riometer absorptions: Implications for determining true precipitation fluxes. *Journal of Geophysical Research: Space Physics*, *118*(12), 7810–7821. https://doi.org/10.1002/2013ja019439

Roederer, J. G. (1967). On the adiabatic motion of energetic particles in a model magnetosphere. *Journal of Geophysical Research*, *72*(3), 981–992. https://doi.org/10.1029/jz072i003p00981

Roederer, J. G., & Lejosne, S. (2018). Coordinates for representing radiation belt particle flux. *Journal of Geophysical Research: Space Physics*, *123*(2), 1381–1387. https://doi.org/10.1002/2017ja025053

Selesnick, R. S. (2015). Measurement of inner radiation belt electrons with kinetic energy above 1 MeV. *Journal of Geophysical Research: Space Physics*, *120*(10), 8339–8349. https://doi.org/10.1002/2015JA021387

Shprits, Y. Y., Horne, R. B., Kellerman, A. C., & Drozdov, A. Y. (2018). The dynamics of Van Allen belts revisited, *Nature Physics*, *14*(2), 102. https://doi.org/10.1038/nphys4350

Shprits, Y. Y., Subbotin, D., Drozdov, A., Usanova, M. E., Kellerman, A., Orlova, K., et al. (2013). Unusual stable trapping of the ultrarelativistic electrons in the Van Allen radiation belts. *Nature Physics*, *9*(11), 699–703. https://doi.org/10.1038/nphys2760

Smith, E. J., Frandsen, A. M. A., Tsurutani, B. T., Thorne, R. M., & Chan, K. W. (1974). Plasmaspheric hiss intensity variations during magnetic storms. *Journal of Geophysical Research*, *79*(16), 2507–2510. https://doi.org/10.1029/ja079i016p02507

Student. (1908). The probable error of a mean. *Biometrika*, *6*(1), 1–25. https://doi.org/10.2307/2331554

Thompson, R. L., Morley, S. K., Watt, C. E. J., Bentley, S. N., & Williams, P. D. (2020). Pro-L *—A probabilistic L * mapping tool for ground observations. *Space Weather*, *19*, 2020SW002602. https://doi.org/10.1029/2020SW002602

Thorne, R. M. (2010). Radiation belt dynamics: The importance of wave-particle interactions. *Geophysical Research Letters*, *37*(22). https://doi.org/10.1029/2010gl044990

Thorne, R. M., Church, S. R., Malloy, W. J., & Tsurutani, B. T. (1977). The local time variation of ELF emissions during periods of substorm activity. *Journal of Geophysical Research*, *82*(10), 1585–1590. https://doi.org/10.1029/ja082i010p01585

Thorne, R. M., Smith, E. J., Burton, R. K., & Holzer, R. E. (1973). Plasmaspheric hiss. *Journal of Geophysical Research*, *78*(10), 1581–1596. https://doi.org/10.1029/ja078i010p01581

Tsurutani, B. T., Smith, E. J., & Thorne, R. M. (1975). Electromagnetic hiss and relativistic electron losses in the inner zone. *Journal of Geophysical Research*, *80*(4), 600–607. https://doi.org/10.1029/ja080i004p00600

Tsyganenko, N. A., & Sitnov, M. I. (2005). Modeling the dynamics of the inner magnetosphere during strong geomagnetic storms. *Journal of Geophysical Research*, *110*(A3). https://doi.org/10.1029/2004JA010798

Van Allen, J. A. (1958). Observation of high intensity radiation by satellites 1958 Alpha and Gamma. *Journal of Jet Propulsion*, *28*(9), 588–592. https://doi.org/10.2514/8.7396

Van Allen, J. A. (1959). The geomagnetically trapped corpuscular radiation. *Journal of Geophysical Research*, *64*(11), 1683–1689. https://doi.org/10.1029/jz064i011p01683

Vassiliadis, D. (2008). Response of the radiation belt electron flux to the solar wind velocity: Parameterization by radial distance and energy. *Journal of Atmospheric and Solar-Terrestrial Physics*, *70*(14), 1810–1828. https://doi.org/10.1016/j.jastp.2008.05.019

Vassiliadis, D., Fung, S. F., & Klimas, A. J. (2005). Solar, interplanetary, and magnetospheric parameters for the radiation belt energetic electron flux. *Journal of Geophysical Research*, *110*(A4), 4201. https://doi.org/10.1029/2004JA010443

Vassiliadis, D., Klimas, A. J., Kanekal, S. G., Baker, D. N., & Weigel, R. S. (2002). Long-term-average, solar cycle, and seasonal response of magnetospheric energetic electrons to the solar wind speed. *Journal of Geophysical Research*, *107*(A11), 1383. https://doi.org/10.1029/2001JA000506

Vassiliadis, D., Klimas, A. J., Weigel, R. S., Baker, D. N., Rigler, E. J., Kanekal, S. G., et al. (2003). Structure of Earth's outer radiation belt inferred from long-term electron flux dynamics. *Geophysical Research Letters*, *30*(19). https://doi.org/10.1029/2003GL017328

Vassiliadis, D., Weigel, R. S., Baker, D. N., Kanekal, S. G., & Klimas, A. J. (2004). Probing the solar wind-inner magnetospheric coupling: Validation of relativistic electron flux models. *Journal of Atmospheric and Solar-Terrestrial Physics*, *66*(15–16), 1399–1409. https://doi.org/10.1016/j.jastp.2004.03.025

Walach, M., & Grocott, A. (2019). SuperDARN observations during geomagnetic storms, geomagnetically active times, and enhanced solar wind driving. *Journal of Geophysical Research: Space Physics*, *124*(7), 5828–5847. https://doi.org/10.1029/2019ja026816

Whittaker, I. C., Clilverd, M. A., & Rodger, C. J. (2014). Characteristics of precipitating energetic electron fluxes relative to the plasmapause during geomagnetic storms. *Journal of Geophysical Research: Space Physics*, *119*(11), 8784–8800. https://doi.org/10.1002/2014ja020446

Yahnina, T. A., & Yahnin, A. G. (2014). Proton precipitation to the equator of the isotropic boundary during the geomagnetic storm on November 20-29, 2003. *Cosmic Research*, *52*(1), 79–85. https://doi.org/10.1134/s0010952514010092